ACS Photonics

Cite This: ACS Photonics 2018, 5, 3526−3533

Letter

pubs.acs.org/journal/apchd5

Indium Tin Oxide Broadband Metasurface Absorber

Sajan Shrestha,[†] Yu Wang,[‡] Adam C. Overvig,[†] Ming Lu,[§] Aaron Stein,[§] Luca Dal Negro,[‡,∥,⊥] and Nanfang Yu*[,†]

[†]Department of Applied Physics and Applied Mathematics, Columbia University, New York, New York, United States

[§]Center for Functional Nanomaterials, Brookhaven National Lab, Upton, New York, United States

[‡]Department of Electrical and Computer Engineering and Photonics Center, [∥]Division of Material Science and Engineering, and [⊥]Department of Physics, Boston University, Boston, Massachusetts 02215, United States

Supporting Information

ABSTRACT: Metamaterials have been designed to achieve a wide range of functionalities. Metamaterial absorbers are of particular interest for various applications such as infrared detectors, emissivity coatings, and photovoltaic cells. Various metamaterial platforms have been demonstrated to achieve perfect absorption and several attempts have been made to extend the absorption bandwidth of such devices. We demonstrate a broadband infrared absorber using an asymmetric Fabry−Perot cavity consisting of a monolithically fabricated two-layer metasurface. Superoctave optical absorption is achieved by tailoring the structure of the metasurface layers and the thickness of the cavity. The device yields absorptance of over 80% from λ = 4−16 μm, while maintaining the performance over a wide range of incident angles. In contrast to most metamaterial absorbers, our metasurface layers are made of customized indium tin oxide (ITO), conferring the advantage of CMOS compatibility compared to previous approaches using noble metals.

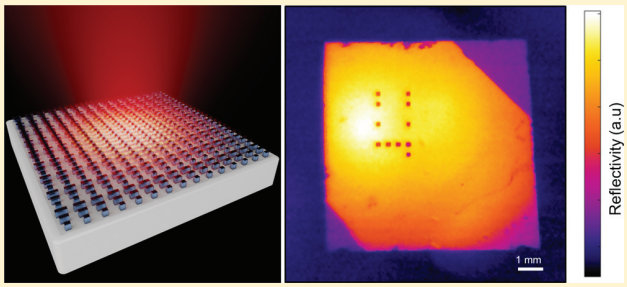

KEYWORDS: *metamaterial absorber, broadband, infrared, nanoresonator, CMOS compatible*

Metamaterials and metasurfaces have generated great interest as tools for studying novel electromagnetic phenomena and have been used to demonstrate a wide range of functionalities,[1] such as wavefront engineering,[2−4] optical modulation,[5,6] and perfect absorption. Metamaterial-based electromagnetic absorbers in particular have applications in solar energy harvesting,[7−9] thermal imaging and sensing,[10−13] and thermal emissivity control.[14−17] Toward these ends, metamaterial platforms have been pursued to achieve near-perfect absorbers in the solar spectrum,[8,18−20] as well as in the infrared[21,22] and terahertz[23] spectral ranges.

Most metamaterial absorbers utilize inherent losses in plasmonic[24] nanostructures to produce large absorption. Plasmonic scatterers embedded in dielectric layers have been reported[25,26] to achieve large absorption enhancement by trapping incident solar radiation. Similarly, coupling light into surface plasmon polaritons in structured metallic films is known to induce large absorption.[27] Tapering a stack of alternative metal and dielectric films produces broadband absorption via excitation of slow light modes.[28,29] Strong local field enhancement in subwavelength plasmonic nanoresonators with tailored electric and magnetic resonances is the most widely used approach to enhance absorption and even achieve near-unity absorption. This platform allows for great flexibility in realizing polarization and incidence angle insensitive absorbers for different wavelength ranges.[21,22,30−33]

While various perfect absorbers utilizing plasmonic nanoresonators have been demonstrated, it is difficult to maintain large absorption over a broad wavelength range due to the limited bandwidth of plasmonic resonances. Multiband absorption[34,35] has been demonstrated by combining different types of plasmonic resonators within a subwavelength unit cell, but the overall bandwidth of absorption is limited by the ability to pack different resonators within a subwavelength period. Multilayered structures[36,37] have been proposed as a solution to this problem, but fabrication of such structures is tedious and designs that can be realized with simpler nanofabrication methods are generally preferred. To that end, a planar structured plasmonic surface optimized by a genetic algorithm to overlap multiple resonances over a chosen wavelength range has been demonstrated[38] to achieve near-unity absorption over an octave bandwidth and maintained over a wide range of incidence angles.

We report here an alternative strategy that, from first-principles, can achieve large absorbance over a superoctave bandwidth by replacing metallic plasmonic elements with nanostructures made of an engineered indium tin oxide (ITO). This material platform is chosen for its tunability of optical response and CMOS compatibility. Our broadband absorbers

Received: June 8, 2018
Published: August 8, 2018

DOI: 10.1021/acsphotonics.8b00781
ACS Photonics 2018, 5, 3526−3533

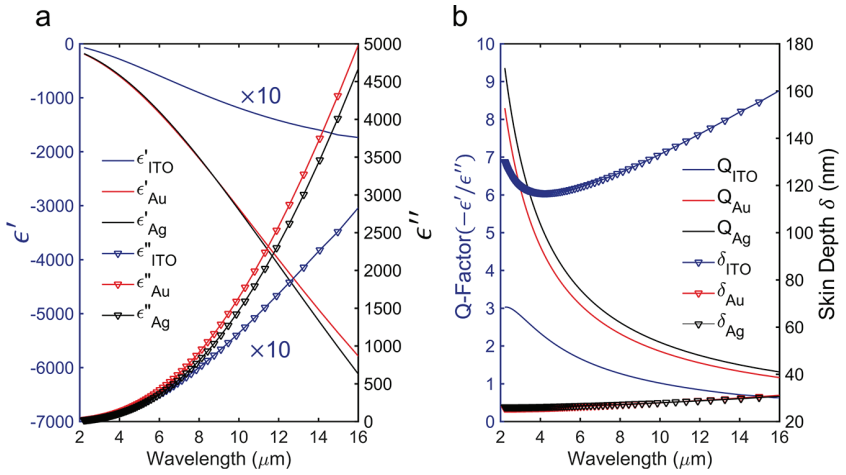

Figure 1. Optical properties of ITO compared to Au and Ag. (a) Real and imaginary parts of permittivities. (b) Quality factor and skin depth of tailored ITO material and noble metals (Au, Ag).

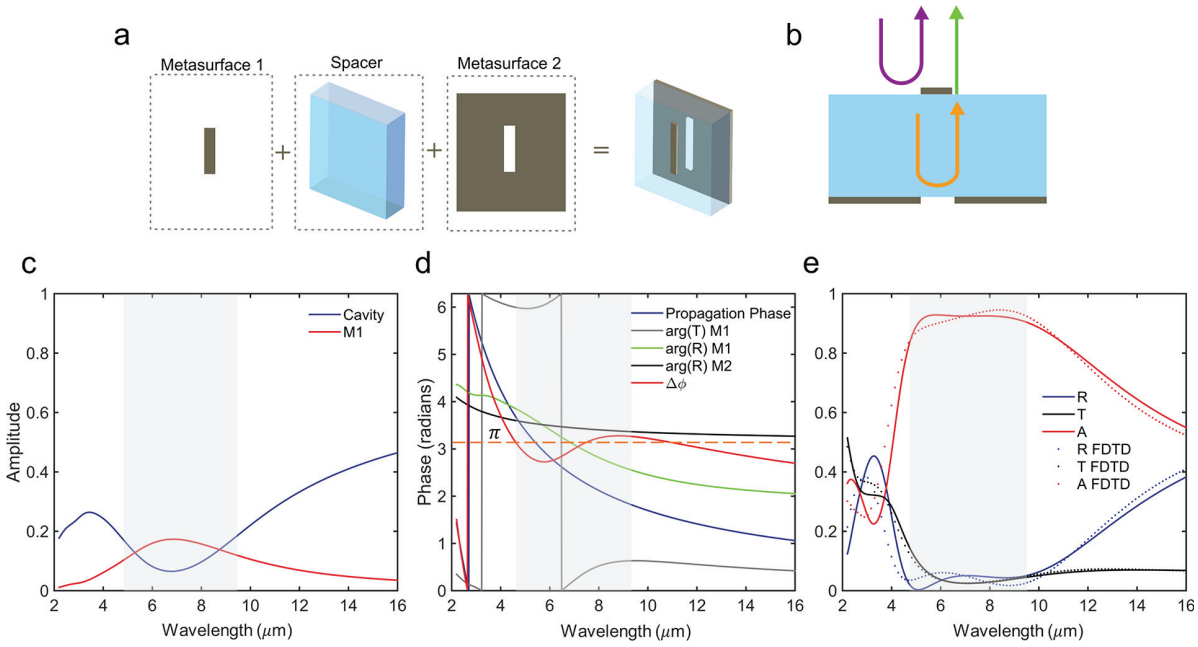

Figure 2. Modeling the metasurface absorber as an asymmetric Fabry–Perot cavity. (a) The metasurface consists of a 2D subwavelength periodic array of lossy rod antennas separated from its Babinet inverse by a dielectric spacer. (b) Overall reflection is approximately the sum of the direct reflection from M1 and the reflection of light during a single round-trip pass through the FP cavity. (c) Amplitudes of the two reflected components as illustrated in (b). The amplitudes are comparable within the shaded wavelength range. (d) The phase difference, $\Delta\phi$, between the two reflected components as illustrated in (b). It is roughly π within the shaded wavelength range. (e) Comparison of reflectance, transmittance, and absorptance spectra predicted by the analytical model for the asymmetric Fabry–Perot cavity (eqs 1–3) and those by FDTD simulations. Shaded region represents the wavelength range over which high absorption is achieved due to a strong destructive interference between the two reflected components.

consist of two Babinet-complementary metasurface layers made of ITO and separated by a dielectric spacer. Each metasurface layer acts as a mirror of a Fabry–Perot cavity. By designing the spectral phase response of the two mirrors in conjunction with the thickness of the cavity, we designed and experimentally demonstrated super broadband absorbers working over more than one octave bandwidth in the mid-infrared.

ITO has been proposed as an alternative plasmonic material in the near-infrared[39] for various applications[40−42] and recently in the mid-infrared band as well. By varying the growth and annealing conditions, its optical properties can be tuned to achieve a negative real part (ϵ') and a small imaginary part (ϵ'') of the dielectric permittivity in the infrared wavelengths.[43,44] The ratio of the real to the imaginary part of dielectric permittivity, which is often used as a figure of merit to determine the quality factor of localized surface plasmon resonance (LSPR) in plasmonic materials, is much larger for noble metals than that for ITO[39] in the near-infrared, and remains slightly greater than that of ITO in the mid-infrared. This leads to a weaker but broader extinction spectrum for plasmonic scatterers made of ITO as compared to those made

DOI: 10.1021/acsphotonics.8b00781
ACS Photonics 2018, 5, 3526−3533

of noble metals. Figure 1a,b shows a comparison of the real and imaginary parts of dielectric permittivity of noble metals (Au and Ag) and the tailored ITO material we used in our metasurfaces. While both the real and imaginary parts of the permittivity are significantly larger for noble metals, the LSPR quality factor of the noble metals is only larger than that of ITO by a factor of ∼2.

Another key material property that must be considered is the optical loss. The plasmonic losses accrued depend on the extent of penetration of light into a material, which is quantified by the skin depth, $\delta \equiv \frac{\lambda}{2\pi \mathrm{Im}[n]}$, where n is the complex refractive index. The skin depth of the noble metals is compared with that of our ITO material in Figure 1b, which shows that electromagnetic waves can penetrate through more than 100 nm of our ITO material but are limited to less than 30 nm in the noble metals. Therefore, despite having much smaller ϵ'', due to the larger skin depth, ITO causes more absorption losses of infrared light, while the noble metals reflect most of the incident infrared light. Thus, by tailoring the growth parameters,[46] in particular, balancing the values of ϵ' and ϵ'', we can realize a material platform that can produce broad resonances with large absorption.

The ITO thin films were deposited using RF magnetron sputtering in a Denton Discovery 18 confocal-target system, with an ITO (99.99% purity) target placed in argon atmosphere at room temperature.[45] The base pressure was 1.0×10^{-7} Torr and the argon gas flow was kept at 12 sccm. The sputtering power was fixed at 200 W, and the thickness of the deposited ITO thin films was measured to be 100 nm. We performed postdeposition annealing of ITO in N_2 at 250 °C for 60 min to tune the optical dispersion of ITO, which was then characterized using a mid-infrared ellipsometer (see Methods). The tunability of ITO optical dispersion with respect to sputtering power and post annealing conditions is shown in Supporting Information.

Broadband absorption in ITO has been reported before[47] by utilizing enhanced light matter interactions at epsilon-near-zero (ENZ) wavelengths for a stack of thin films of ITO, each with a different ENZ wavelength.[48] However, this requires excitation in an attenuated total reflection configuration and the absorption occurs only around the ENZ wavelengths (1.3−1.9 μm). In contrast, we use a coating of ITO operating well above the ENZ wavelength, which therefore does not rely on the field enhancement associated with the ENZ condition and hence can achieve enhanced absorption over a significantly larger wavelength range by utilizing a structured ITO metasurface.

In this paper, we report a super broadband metamaterial absorber with absorptance values of over 75% spanning from λ = 4 to 16 μm. We achieve large absorbance across the entire band using a resonant cavity based on a dual-layer metasurface. Two lossy ITO metasurface mirrors enclose a dielectric spacer forming a Fabry−Perot (FP) cavity. By tailoring the electromagnetic response of the metasurface mirrors and thickness of the cavity, we produce cavity resonances that satisfy the destructive interference condition for reflected waves over a large bandwidth.

Figure 2a depicts three layers that form the asymmetric FP cavity. Metasurface 1 (M1) is a two-dimensional array of rod antennas; its Babinet inverse, Metasurface 2 (M2) forms the second mirror. Together they enclose a dielectric spacer of thickness d and effective index n_{eff}. Each meta-unit that makes up these metasurfaces are deeply subwavelength and optically thin. Additionally, the two metasurface layers are assumed to operate independently (i.e., there is negligible near-field coupling due to the spacing between them). Hence, we can treat these layers as optically thin interfaces with tailored optical responses. The reflection and transmission coefficients of the resulting cavity are respectively given by[49]

$$r = \frac{r_1 + (t_1 t_1' - r_1 r_1') r_2' e^{-i\delta}}{1 - r_1' r_2' e^{-i\delta}} \tag{1}$$

and

$$t = \frac{t_1 t_2' e^{-i\delta/2}}{1 - r_1' r_2' e^{-i\delta}} \tag{2}$$

where $\delta = \frac{4\pi n_{\mathrm{eff}} d \cos\theta}{\lambda}$, $r_1(t_1)$ and $r_2(t_2)$ are the reflection (transmission) coefficients of M1 and M2, respectively. The primes represent the coefficients when the direction of propagation is reversed. Overall absorptance,

$$A = 1 - |t|^2 - |r|^2 \tag{3}$$

can be calculated by obtaining properties of the constituent layers by using finite-difference time-domain (FDTD) simulations. A similar treatment of metamaterials as an assembly of multiple metasurfaces has been reported previously.[50]

The designs of the metasurfaces are aimed at suppressing overall reflection and transmission. Direct reflection from M1 and the reflection from the FP cavity represent the two channels contributing to the overall metamaterial reflection as shown in Figure 2b. We employ a basic design principle aiming to maximize the bandwidth over which the destructive interference condition occurs: when the electromagnetic waves corresponding to the two paths are equal in amplitude and out of phase. We calculate the absorption spectrum of a metasurface consisting of an array of ITO rod antennas (length of 1400 nm, width of 400 nm, and thickness of 100 nm) as M1, its Babinet inverse as M2, and a dielectric spacer (thickness of 1400 nm and refractive index of 1) using our model and compare it with FDTD simulation of the same structure. The exclusion of loss in the dielectric spacer (which is present in the final device to be shown later) is found to make little difference in the analytically calculated spectrum, which demonstrates that the primary loss mechanism is due to M1 and M2. The transmittance through the device is small because M2 acts as an excellent mirror. Figure 2c shows analytically calculated amplitudes of the direct reflection from M1 and the reflection from the FP cavity (assuming a single round-trip pass through the cavity). Figure 2d shows the phase difference between these two components, given by

$$\Delta\phi = \arg(r_1) - [\arg(t_1) + 2\pi n_{\mathrm{eff}} d/\lambda + \arg(r_2)]$$

The highlighted region in Figure 2c represents the wavelength range where the amplitudes of the two reflected components are comparable, while their phase difference is close to π. This will lead to strong destructive interference at the reflection port and, as a result, large absorption over the corresponding bandwidth. This is confirmed by our analytical model (eqs 1−3) and FDTD simulations, which are presented in Figure 2e. The model successfully reproduces reflection, transmission, and absorption spectra obtained from FDTD

DOI: 10.1021/acsphotonics.8b00781
ACS Photonics 2018, 5, 3526−3533

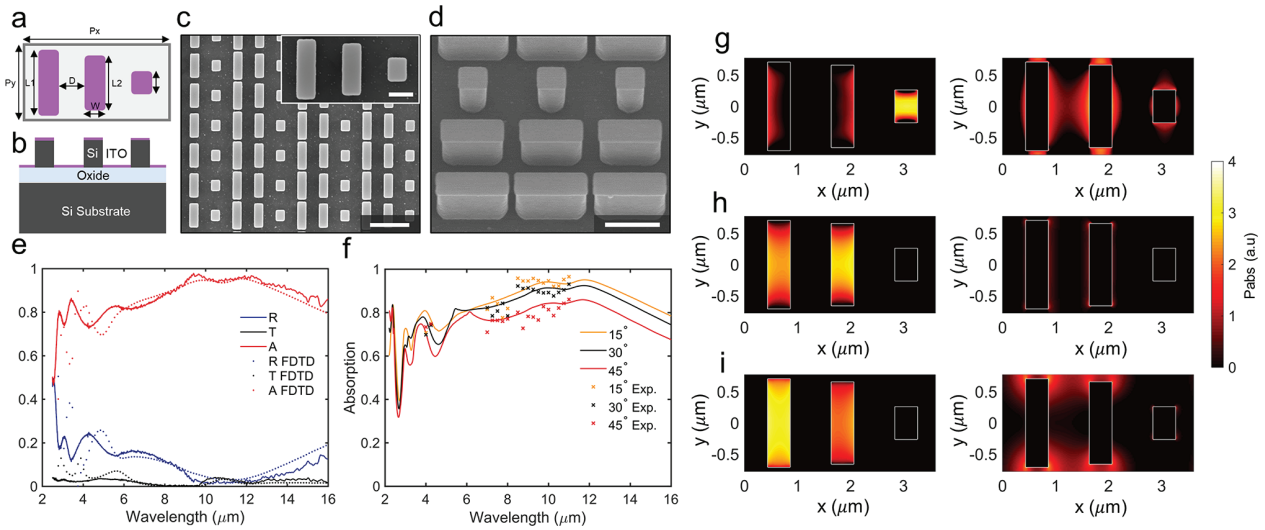

Figure 3. Design and performance of a broadband polarization-dependent infrared metasurface absorber. (a) Top view of the unit cell of the metasurface. (b) Cross-sectional view of the unit cell of the metasurface. (c) SEM image of a fabricated device (Scale bar: 2000 nm). Inset: one unit cell (scale bar: 500 nm). (d) SEM image taken at an oblique angle of the fabricated device (scale bar: 1000 nm). (e) Measured and simulated reflection, transmission, and absorption spectra of the metasurface absorber. (f) Simulated and measured absorption spectra at different incident angles. (g–i) Spatial distributions of absorbed optical power on the plane of M1 (left) and M2 (right) at λ = 4, 6.25, and 10 μm, respectively.

simulations, of the combined metamaterial, validating the description of the device as an asymmetrical FP cavity.

We apply our understanding of the broadband absorption process to design a device with large absorptance spanning multiple octaves in the mid-infrared. We overlap resonances of multiple ITO antennas of different lengths, each antenna supporting a different resonance wavelength, and a correspondingly different wavelength range over which the destructive interference condition can be satisfied. Figure 3a shows a single period of the unit cell of a polarization dependent absorber with all the design parameters. This design is based on three antennas of different lengths and is a simple extension of the one based on a single antenna discussed above. The cross-section of the unit cell illustrated in Figure 3b shows that M1 and M2 are separated by an array of silicon nanopillars with subwavelength periodicity, acting as the dielectric spacer. The metasurface is fabricated on a Silicon on Insulator (SOI) chip, which has a 2.2 μm buried oxide layer and a 1.4 μm device layer. This design allows us to fabricate both the ITO rod antenna array (M1) and its Babinet inverse (M2) with a single lithographic and etch step followed by deposition of a thin film of ITO and post deposition annealing processes (see Methods, Nanofabrication). While the array of silicon nanopillars is an unconventional choice for a spacer, it can be modeled as a dielectric slab with an effective index due to the deep subwavelength size of the constituent elements. While not shown in Figure 3b, the side walls of the pillars are covered with ITO due to the conformal nature of the sputtering method used. This fact is taken into account in our numerical simulations. The device parameters are determined by optimization using FDTD simulations to obtain large absorptance in the wavelength range of 4–16 μm. Keeping the thickness of the ITO layer to be 100 nm, we simulate single antennas of various lengths, widths, periodicities, and spacings between its Babinet inverse. For the polarization-dependent design, we search for a single antenna element that achieves the largest absorption over the largest possible bandwidth using FDTD simulations. We then supplement the first antenna by adding additional antennas of different lengths to increase absorption in the wavelength ranges where the absorption provided by the first antenna is weak, while keeping the cavity spacing fixed. Since the cavity spacing has been fixed, the absorption produced due to destructive interference resulting from these new antennas at various wavelengths might not be complete, leading to a slightly lower values of absorption. Using this very simple scheme, we arrive at a three-element unit cell with lengths, L_1 = 1450 nm, L_2 = 1250 nm, L_3 = 550 nm, widths, W = 400 nm, interantenna gap, D = 700 nm, periods P_x = 3600 nm, and P_y = 1550 nm, and cavity spacing of 1400 nm (Figure 3a). SEM images of the fabricated device are shown in Figure 3c,d.

We measure the reflection (R) and transmission (T) spectra of fabricated devices using Fourier Transform Infrared (FTIR) spectroscopy and calculate the absorption spectra defined by eq 3. Both the reflection and transmission measurements are carried out at normal incidence with linear polarization in the direction along the antenna rod. The results of FTIR measurements are plotted in Figure 3e along with the corresponding results obtained from FDTD simulations. We observe super broadband absorptance of over 75% across the entire wavelength range of 4–16 μm, a two-octave span across the spectral region corresponding to thermal radiation. We also fabricate and characterize periodic arrays of the individual antennas that compose the polarization-dependent metasurface absorber. The resulting spectra (see Supporting Information, Figure S2) clearly show broad resonances centered at λ = 6, 10, and 13 μm supported by the arrays of antennas with length of 550, 1250, and 1450 nm, respectively, with a good agreement with FDTD simulations. But the overall bandwidth of large absorption is limited around these resonance peaks unlike the broadband operation shown by the multiplexed design in Figure 3a.

We calculate spatial distributions of absorbed power per unit volume, $P_{abs} \propto |E|^2\epsilon''$, and the results are shown in Figure 3g–i. We observe that absorption on the M1 layer (ITO rods) is larger than that on the M2 layer (ITO apertures). This is

DOI: 10.1021/acsphotonics.8b00781
ACS Photonics 2018, 5, 3526–3533

expected since the M2 layer is not specifically designed to be resonant at any wavelength and acts mostly as a mirror. We also observe that light with longer wavelengths is primarily absorbed by longer antennas and that the largest absorption occurs at the edges of the antenna rods.

We conduct FDTD simulations to investigate absorption as a function of incidence angle. Figure 3f shows that broadband high absorption is retained for incident angles of up to 30° and absorptance starts to decrease at an incident angle of 45°. We have validated these numerical simulations with measurements in the wavelength range of 4−11 μm (see Methods for details).

Using the same design principles, we also demonstrate a polarization-independent absorber. The unit cell of the metasurface is shown in Figure 4a and consists of two types of rod antennas arranged symmetrically with the following parameters: L = 520 nm, W = 300 nm, D = 400 nm, and P = 1200 nm. The vertical cross-section of the unit cell is shown in Figure 4b, where the cavity spacing is again 1400 nm. Figure 4c,d show SEM images of a fabricated device. Figure 4g,h shows the spatial distributions of absorbed power of the polarization-independent unit cell at λ = 4 and 12 μm, respectively. We see strong absorption around the region where the horizontal and vertical antennas meet for both wavelengths on both the M1 and M2 planes. The central square antenna primarily absorbs light of shorter wavelengths. Unlike the polarization-dependent design, the power absorbed in the M2 layer is comparable to that absorbed in the M1 layer.

Measured spectra of the polarization-independent metasurface absorber are shown in Figure 4e. In this case, we use unpolarized light as the source of illumination. We observe a large absorption of greater than 80% over the entire wavelength range of 6−16 μm. The overall performance of the fabricated device agrees with FDTD simulations, and we attribute the discrepancy in the position of some resonances to fabrication errors. Similar to the polarization-dependent unit cell, this design maintains broadband high absorptance for incident angles of up to 30° as shown by FDTD simulations and experiment in Figure 4f. Note that we obtain such performance without using complex optimization schemes for the design and complicated device fabrication techniques.

We further investigate the thermal emissivity of the fabricated metasurface absorbers using a thermal camera. Emissivity of samples can be obtained by heating the samples with a reference material with known emissivity. At thermal equilibrium, the temperature reported by the thermal camera must be the same for both materials, which serves as a method to solve for the emissivity of the unknown sample. Note that, for accurate measurements of sample temperature, external contributions (i.e., ambient thermal radiation reflected from metasurface absorbers and thermal radiation generated by imaging optics) must be subtracted from the total thermal radiation impinging on the camera sensor (see Methods and Supporting Information, Figure S3a for details).

The thermal images of the devices heated to 150 °C are shown in Figure 5a (see Figure S3b for thermal images of samples at room temperature) where the metasurface absorbers are the regions with bright yellow coloration. Thermal image of the reference (see Figure S3c) material (black electrical tape) gives us a reference temperature (T_R) of 110 °C. Figure 5b shows plots of calculated temperature as a

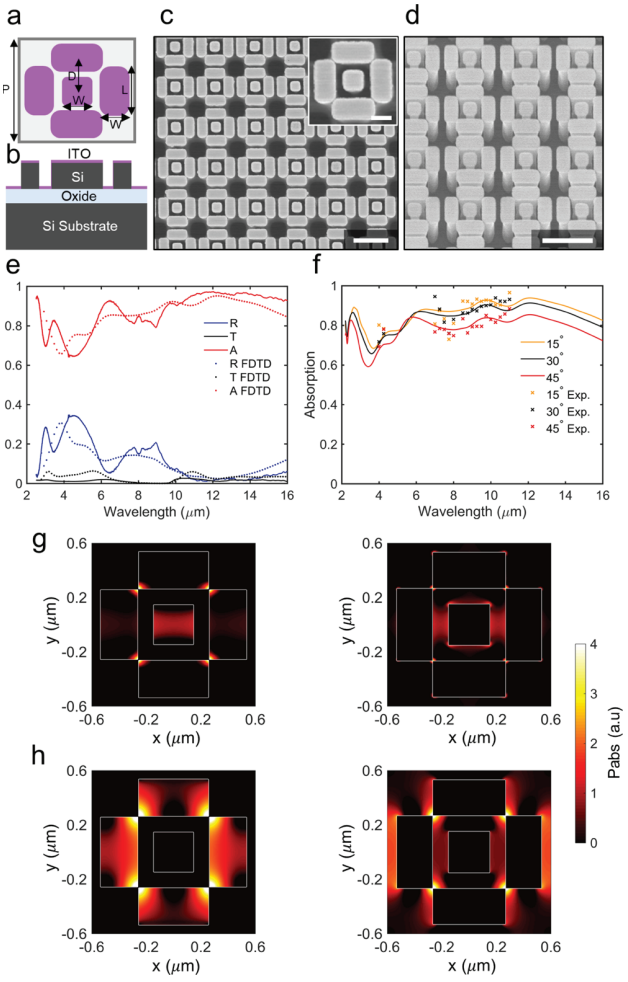

Figure 4. Design and performance of a broadband polarization-independent infrared metasurface absorber. (a) Top view of the unit cell of the metasurface. (b) Cross-sectional view of the unit cell of the metasurface. (c) SEM image of a fabricated device (scale bar: 1000 nm). Inset: one unit cell (scale bar: 300 nm). (d) SEM image taken at an oblique angle of a fabricated device (scale bar: 1000 nm). (e) Measured and simulated reflection, transmission, and absorption spectra of the metasurface absorber. (f) Simulated and measured absorption spectra at different incident angles. (g, h) Spatial distributions of absorbed optical power on the plane of M1 (left) and M2 (right) at λ = 5.96 and 12 μm, respectively. Polarization of incident light is along y-axis.

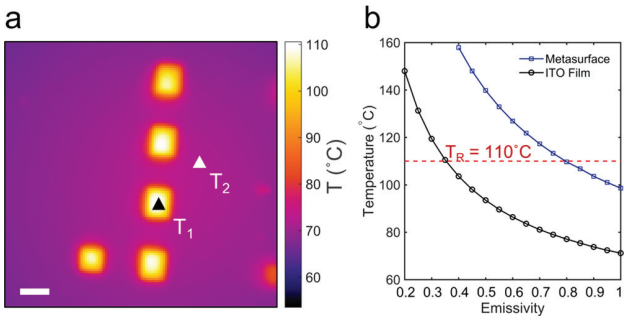

Figure 5. Emissivity measurements using a thermal camera. (a) Magnified thermal image of devices where T_1 and T_2 representing temperatures of the metasurface absorber and the unpatterned ITO film, respectively. Scale bar: 200 μm. (b) T_1 and T_2 as a function of emissivity.

DOI: 10.1021/acsphotonics.8b00781
ACS Photonics 2018, 5, 3526−3533

function of emissivity for spots on the metasurface absorber (T_1) and the ITO thin film surrounding it (T_2) in Figure 5a. The emissivity values that return T_R are the correct value of emissivity for the two spots. We observe from the figure that emissivity of our metasurface absorbers is >0.8 and that of the unpatterned ITO film is around 0.3. These values agree qualitatively with absorptance values retrieved from the FTIR measurements.

In conclusion, we have experimentally demonstrated super-broadband metasurface infrared absorbers based on engineered ITO that maintain large absorptance and broadband performance over a wide range of incidence angles. The engineered optical properties of ITO enable the creation of metasurfaces that have broad antenna resonances. We developed an asymmetric Fabry−Perot model to describe the operation principle of our absorbers as a pair of metasurfaces acting as a broadband cavity. Results of the model agree well with FDTD simulations. We used the simulation results to optimize the unit cell of the metasurface absorber and experimentally achieved over 80% absorptance in the entire 4−16 μm wavelength range, a significant improvement over similar works reported previously. Using FDTD simulations, we showed that this performance is maintained for a wide range of incidence angles (±30°). We have thus successfully demonstrated an alternative method of achieving super broadband absorbers of infrared light using ITO with engineered optical properties. Using thermal imaging techniques, we also obtained thermal emissivity of our fabricated devices. Our approach opens up new possibilities of realizing active optoelectronic devices operating in the mid-infrared such as active thermal emitters and imaging sensors that can be fabricated using CMOS compatible techniques.

METHODS

Numerical Simulations. Finite-difference time-domain (FDTD) simulations of various unit cell designs were carried out using Lumerical FDTD Solutions. We used periodic boundary conditions in x and y and perfectly match layer (PML) conditions in z for all simulations. Material properties obtained from mid-IR ellipsometry (IR-VASE) were used to simulate the tailored ITO films. The Palik library was used to simulate the dispersion of silicon and silicon dioxide. We obtained reflection (R) and transmission (T) spectra from the simulations of the unit cells and calculated the absorption using the relation $A = 1 - T - R$.

To obtain absorptance at non-normal incidence, Broadband Fixed Angle Source Technique (BFAST) was used in the FDTD simulation, which removes the wavelength dependence of injection angles from the simulation.

Angular Reflectivity Measurements. The Fourier Transform Infrared (FTIR) spectroscopy system we used for measurement at normal incidence cannot perform similar measurements at non-normal incidence. We built a separate setup for those measurements, which uses a tunable Quantum Cascade Laser (QCL) as the source. The laser (MIRcat −1400, Daylight Solutions) has three tunable QCLs operating in the wavelength range of 3.94−4.39, 6.89−9, and 7.96−11 μm, respectively. We are therefore limited from conducting angular measurements beyond 11 μm. The light from the laser is focused onto the sample using an off-axis parabolic mirror of an effective focal length of 50 mm. The sample is mounted on a stage capable of rotating about a central axis. The reflected light is measured using a power meter (Ophir Optronics Solutions).

Nanofabrication. The metasurface absorber was fabricated on a silicon-on-insulator substrate with the device layer of 1400 nm and a buffered oxide layer of 2200 nm. Double layer PMMA 495 K A4 and 950 A2 were spun on the chip at 4000 rpm for 60 s and baked at 180 °C for 8 and 2 min, respectively. The unit cell patterns were defined on the resist layer using a JEOL JBX-6300FS electron beam lithography system. After development of the resist in 3:1 isopropyl alcohol (IPA)/deionized water (DI) solution for 2 min, 40 nm of chromium was evaporated on it using electron beam evaporation and followed by lift-off in Remover PG. The pattern was finally transferred to silicon by inductively coupled plasma etching in a mixture of SF_6 (40 sccm) and O_2 (16 sccm) at −100 °C. The chromium hard mask was wet etched in Transene. Finally, 100 nm of ITO was deposited using RF magnetron sputtering in a Denton Discovery 18 confocal-target system, with ITO (99.99% purity) target in Ar atmosphere at room temperature. The property of the deposited ITO was then tuned by postdeposition annealing using a Mellen thermal furnace at 250 °C for 1 h in nitrogen atmosphere.

Characterization. ITO films grown under various growth and postannealing conditions were characterized using a mid-infrared J. A. Woollam variable angle spectroscopic ellipsometer (VASE). The reflection and transmission spectroscopic measurements were carried out using a Bruker Scientific Vertex 70v Fourier transform infrared spectrometer equipped with a globar source and a liquid-nitrogen-cooled Mercury Cadmium Telluride (MCT) detector (λ = 2.5−16 μm).

For emissivity characterization, fabricated devices were imaged using a thermal camera (FLIR T640) equipped with a Germanium zoom-in lens. A zinc selenide (ZnSe) lens (Thorlabs) with 0.42 NA was used between the sample and the camera for magnification.

The total thermal radiation received by the camera is given by

$$W_{tot} = \tau\epsilon_s\sigma T_s^4 + \tau(1-\epsilon_s)\sigma T_a^4 + (1-\tau)\sigma T_{lens}^4 \quad \text{(M1)}$$

where ϵ_s is emissivity of the sample, T_s, T_a, and T_{lens} are, respectively, temperatures of the sample, ambient, and ZnSe lens; σ is the Stefan−Boltzmann constant; τ is the power transmissivity of thermal radiation through the ZnSe lens and is taken to be 0.8. The first term on the righthand side of eq M1 represents thermal radiation generated by the sample and transmitted through the ZnSe lens; the second term represents ambient thermal radiation reflected by the sample; the third term represents thermal radiation from the ZnSe lens itself. The camera reports temperature of the sample by solving T_s from the above equation, that is

$$T_s = \left[\frac{\frac{W_{tot}}{\sigma} - \tau(1-\epsilon_s)T_a^4 - (1-\tau)T_{lens}^4}{\epsilon_s\tau}\right]^{1/4} \quad \text{(M2)}$$

We used the following three steps to derive the emissivity of our samples.

Step 1: Experimentally obtain T_a: The primary contribution to the ambient radiation is thermal radiation generated by the thermal camera, because of its close proximity to the sample. Therefore, we shall not take lab ambient temperature 25 °C as T_a. To experimentally determine T_a, we used a flat silver mirror

DOI: 10.1021/acsphotonics.8b00781
ACS Photonics 2018, 5, 3526−3533

as the sample and placed it on a hot plate set to 150 °C. The camera was focused onto the surface of the mirror. The latter has near-zero emissivity; therefore, the reading of the thermal camera only has two contributions:

$$W_{\mathrm{Ag\_mirror}} = \tau\sigma T_{\mathrm{a}}^4 + (1-\tau)\sigma T_{\mathrm{lens}}^4 \quad \text{(M3)}$$

We measured T_{lens} to be 35 °C and the reading from the thermal camera gives us T_{a}:

$$T_{\mathrm{a}} = \left[\frac{W_{\mathrm{Ag\_mirror}}}{\sigma\tau} - \frac{(1-\tau)}{\tau}T_{\mathrm{lens}}^4\right]^{1/4} \quad \text{(M4)}$$

Step 2: Experimentally obtain T_{s}: We replaced the silver mirror from the hot plate with our sample. A piece of black electrical tape with an emissivity of $\epsilon_{\mathrm{tape}} = 0.97$ was attached to the top surface of this sample. We assumed that eventually the tape reaches the same temperature as that of the sample, T_{s}. T_{a} obtained from Step 1 was input into the camera, which calculates T_{s} (see Supporting Information, Figure S3c) using an equation similar to eq M2:

$$T_{\mathrm{s}} = \left[\frac{\frac{W_{\mathrm{tape}}}{\sigma} - \tau(1-\epsilon_{\mathrm{tape}})T_{\mathrm{a}}^4 - (1-\tau)T_{\mathrm{lens}}^4}{\epsilon_{\mathrm{tape}}\tau}\right]^{1/4} \quad \text{(M5)}$$

Step 3: Experimentally obtain ϵ_{meta}, emissivity of the metasurface absorbers: We input a series of ϵ_{meta}, ranging from 0.2 to 1.0, into the thermal camera, which produces a corresponding series of temperature using

$$T_{\mathrm{s}} = \left[\frac{\frac{W_{\mathrm{meta}}}{\sigma} - \tau(1-\epsilon_{\mathrm{meta}})T_{\mathrm{a}}^4 - (1-\tau)T_{\mathrm{lens}}^4}{\epsilon_{\mathrm{meta}}\tau}\right]^{1/4} \quad \text{(M6)}$$

The value of ϵ_{meta} that yields the same temperature as that of the black tape, T_{s}, obtained in Step 2, should be the real thermal emissivity of the metasurface device (Figure 5b).

■ ASSOCIATED CONTENT

Supporting Information

The Supporting Information is available free of charge on the ACS Publications website at DOI: 10.1021/acsphotonics.8b00781.

Tunability of optical property of ITO; FTIR measurements of individual rod elements; Details of emissivity measurements (PDF).

■ AUTHOR INFORMATION

Corresponding Author

*E-mail: ny2214@columbia.edu.

ORCID

Sajan Shrestha: 0000-0002-3369-2248

Adam C. Overvig: 0000-0002-7912-4027

Notes

The authors declare no competing financial interest.

■ ACKNOWLEDGMENTS

The work was supported by the Air Force Office of Scientific Research (Nos. FA9550-14-1-0389 and FA9550-16-1-0322), and the National Science Foundation (No. ECCS-1307948). A.C.O. acknowledges support from the NSF IGERT program (No. DGE-1069240). L.D.N. would like to thank the support of the NSF EAGER program under Award No. ECCS 1643118 and the NSF program under Award No. DMR 1709704. Research was carried out in part at the Center for Functional Nanomaterials, Brookhaven National Laboratory, which is supported by the U.S. Department of Energy, Office of Basic Energy Sciences (Contract No. DE-SC0012704).

■ REFERENCES

(1) Zheludev, N.; Kivshar, Y. From Metamaterials To Metadevices. *Nat. Mater.* **2012**, *11*, 917−924.

(2) Yu, N.; Capasso, F. Flat Optics With Designer Metasurfaces. *Nat. Mater.* **2014**, *13*, 139−150.

(3) Mohammadi Estakhri, N.; Alù, A. Wave-Front Transformation With Gradient Metasurfaces. *Phys. Rev. X* **2016**, *6*, 6.

(4) Kim, M.; Jeong, J.; Poon, J.; Eleftheriades, G. Vanadium-Dioxide-Assisted Digital Optical Metasurfaces For Dynamic Wavefront Engineering. *J. Opt. Soc. Am. B* **2016**, *33*, 980.

(5) Chen, H.; Padilla, W.; Cich, M.; Azad, A.; Averitt, R.; Taylor, A. A Metamaterial Solid-State Terahertz Phase Modulator. *Nat. Photonics* **2009**, *3*, 148−151.

(6) Chen, H.; Padilla, W.; Zide, J.; Gossard, A.; Taylor, A.; Averitt, R. Active Terahertz Metamaterial Devices. *Nature* **2006**, *444*, 597−600.

(7) Wu, C.; Neuner, B., III; John, J.; Milder, A.; Zollars, B.; Savoy, S.; Shvets, G. Metamaterial-Based Integrated Plasmonic Absorber/Emitter For Solar Thermo-Photovoltaic Systems. *J. Opt.* **2012**, *14*, 024005.

(8) Zhu, J.; Yu, Z.; Burkhard, G.; Hsu, C.; Connor, S.; Xu, Y.; Wang, Q.; McGehee, M.; Fan, S.; Cui, Y. Optical Absorption Enhancement In Amorphous Silicon Nanowire And Nanocone Arrays. *Nano Lett.* **2009**, *9*, 279−282.

(9) Wang, H.; Prasad Sivan, V.; Mitchell, A.; Rosengarten, G.; Phelan, P.; Wang, L. Highly Efficient Selective Metamaterial Absorber For High-Temperature Solar Thermal Energy Harvesting. *Sol. Energy Mater. Sol. Cells* **2015**, *137*, 235−242.

(10) Talghader, J.; Gawarikar, A.; Shea, R. Spectral Selectivity In Infrared Thermal Detection. *Light: Sci. Appl.* **2012**, *1*, e24.

(11) Landy, N.; Bingham, C.; Tyler, T.; Jokerst, N.; Smith, D.; Padilla, W. Design, Theory, And Measurement Of A Polarization-Insensitive Absorber For Terahertz Imaging. *Phys. Rev. B: Condens. Matter Mater. Phys.* **2009**, *79*, na.

(12) Liu, N.; Mesch, M.; Weiss, T.; Hentschel, M.; Giessen, H. Infrared Perfect Absorber And Its Application As Plasmonic Sensor. *Nano Lett.* **2010**, *10*, 2342−2348.

(13) Li, W.; Valentine, J. Metamaterial Perfect Absorber Based Hot Electron Photodetection. *Nano Lett.* **2014**, *14*, 3510−3514.

(14) Dyachenko, P.; Molesky, S.; Petrov, A.; Störmer, M.; Krekeler, T.; Lang, S.; Ritter, M.; Jacob, Z.; Eich, M. Controlling Thermal Emission With Refractory Epsilon-Near-Zero Metamaterials Via Topological Transitions. *Nat. Commun.* **2016**, *7*, 11809.

(15) Liu, X.; Tyler, T.; Starr, T.; Starr, A.; Jokerst, N.; Padilla, W. Taming The Blackbody With Infrared Metamaterials As Selective Thermal Emitters. *Phys. Rev. Lett.* **2011**, *107*, na.

(16) D'Aguanno, G.; Mattiucci, N.; Alù, A.; Argyropoulos, C.; Foreman, J.; Bloemer, M. Thermal Emission From A Metamaterial Wire Medium Slab. *Opt. Express* **2012**, *20*, 9784.

(17) Fu, C.; Zhang, Z. Thermal Radiative Properties Of Metamaterials And Other Nanostructured Materials: A Review. *Frontiers of Energy and Power Engineering in China* **2009**, *3*, 11−26.

(18) Hedayati, M.; Javaherirahim, M.; Mozooni, B.; Abdelaziz, R.; Tavassolizadeh, A.; Chakravadhanula, V.; Zaporojtchenko, V.;

DOI: 10.1021/acsphotonics.8b00781
ACS Photonics 2018, 5, 3526−3533

Strunkus, T.; Faupel, F.; Elbahri, M. Design Of A Perfect Black Absorber At Visible Frequencies Using Plasmonic Metamaterials. *Adv. Mater.* **2011**, *23*, 5410−5414.
(19) Cao, T.; Wei, C.; Simpson, R.; Zhang, L.; Cryan, M. Broadband Polarization-Independent Perfect Absorber Using A Phase-Change Metamaterial At Visible Frequencies. *Sci. Rep.* **2015**, *4*, na.
(20) Wang, H.; Wang, L. Perfect Selective Metamaterial Solar Absorbers. *Opt. Express* **2013**, *21*, A1078.
(21) Liu, X.; Starr, T.; Starr, A.; Padilla, W. Infrared Spatial And Frequency Selective Metamaterial With Near-Unity Absorbance. *Phys. Rev. Lett.* **2010**, *104*, na.
(22) Ding, F.; Dai, J.; Chen, Y.; Zhu, J.; Jin, Y.; Bozhevolnyi, S. Broadband Near-Infrared Metamaterial Absorbers Utilizing Highly Lossy Metals. *Sci. Rep.* **2016**, *6*, na.
(23) Diem, M.; Koschny, T.; Soukoulis, C. Wide-Angle Perfect Absorber/Thermal Emitter In The Terahertz Regime. *Phys. Rev. B: Condens. Matter Mater. Phys.* **2009**, *79*, na.
(24) Atwater, H.; Polman, A. Plasmonics For Improved Photovoltaic Devices. *Nat. Mater.* **2010**, *9*, 205−213.
(25) Li, B.; Lin, J.; Lu, J.; Su, X.; Li, J. Light Absorption Enhancement In Thin-Film Solar Cells By Embedded Lossless Silica Nanoparticles. *J. Opt.* **2013**, *15*, 055005.
(26) Carretero-Palacios, S.; Calvo, M.; Míguez, H. Absorption Enhancement In Organic−Inorganic Halide Perovskite Films With Embedded Plasmonic Gold Nanoparticles. *J. Phys. Chem. C* **2015**, *119*, 18635−18640.
(27) Tvingstedt, K.; Persson, N.; Inganäs, O.; Rahachou, A.; Zozoulenko, I. Surface Plasmon Increase Absorption In Polymer Photovoltaic Cells. *Appl. Phys. Lett.* **2007**, *91*, 113514.
(28) Ding, F.; Jin, Y.; Li, B.; Cheng, H.; Mo, L.; He, S. Ultrabroadband Strong Light Absorption Based On Thin Multi-layered Metamaterials. *Laser & Photonics Reviews* **2014**, *8*, 946−953.
(29) Cui, Y.; Fung, K.; Xu, J.; Ma, H.; Jin, Y.; He, S.; Fang, N. Ultrabroadband Light Absorption By A Sawtooth Anisotropic Metamaterial Slab. *Nano Lett.* **2012**, *12*, 1443−1447.
(30) Landy, N.; Sajuyigbe, S.; Mock, J.; Smith, D.; Padilla, W. Perfect Metamaterial Absorber. *Phys. Rev. Lett.* **2008**, *100*, na.
(31) Aydin, K.; Ferry, V.; Briggs, R.; Atwater, H. Broadband Polarization-Independent Resonant Light Absorption Using Ultrathin Plasmonic Super Absorbers. *Nat. Commun.* **2011**, *2*, 517.
(32) Ye, Y.; Jin, Y.; He, S. Omnidirectional, Polarization-Insensitive And Broadband Thin Absorber In The Terahertz Regime. *J. Opt. Soc. Am. B* **2010**, *27*, 498.
(33) Mandal, J.; Wang, D.; Overvig, A.; Shi, N.; Paley, D.; Zangiabadi, A.; Cheng, Q.; Barmak, K.; Yu, N.; Yang, Y. Scalable, "Dip-And-Dry" Fabrication Of A Wide-Angle Plasmonic Selective Absorber For High-Efficiency Solar-Thermal Energy Conversion. *Adv. Mater.* **2017**, *29*, 1702156.
(34) Zhang, B.; Zhao, Y.; Hao, Q.; Kiraly, B.; Khoo, I.; Chen, S.; Huang, T. Polarization-Independent Dual-Band Infrared Perfect Absorber Based On A Metal-Dielectric-Metal Elliptical Nanodisk Array. *Opt. Express* **2011**, *19*, 15221.
(35) Cui, Y.; Xu, J.; Hung Fung, K.; Jin, Y.; Kumar, A.; He, S.; Fang, N. A Thin Film Broadband Absorber Based On Multi-Sized Nanoantennas. *Appl. Phys. Lett.* **2011**, *99*, 253101.
(36) Xiong, H.; Hong, J.; Luo, C.; Zhong, L. An Ultrathin And Broadband Metamaterial Absorber Using Multi-Layer Structures. *J. Appl. Phys.* **2013**, *114*, 064109.
(37) Wen, D.; Yang, H.; Ye, Q.; Li, M.; Guo, L.; Zhang, J. Broadband Metamaterial Absorber Based On A Multi-Layer Structure. *Phys. Scr.* **2013**, *88*, 015402.
(38) Bossard, J.; Lin, L.; Yun, S.; Liu, L.; Werner, D.; Mayer, T. Near-Ideal Optical Metamaterial Absorbers With Super-Octave Bandwidth. *ACS Nano* **2014**, *8*, 1517−1524.
(39) West, P.; Ishii, S.; Naik, G.; Emani, N.; Shalaev, V.; Boltasseva, A. Searching For Better Plasmonic Materials. *Laser & Photonics Reviews* **2010**, *4*, 795−808.
(40) Capretti, A.; Wang, Y.; Engheta, N.; Dal Negro, L. Enhanced Third-Harmonic Generation In Si-Compatible Epsilon-Near-Zero Indium Tin Oxide Nanolayers. *Opt. Lett.* **2015**, *40*, 1500.
(41) Capretti, A.; Wang, Y.; Engheta, N.; Dal Negro, L. Comparative Study Of Second-Harmonic Generation From Epsilon-Near-Zero Indium Tin Oxide And Titanium Nitride Nanolayers Excited In The Near-Infrared Spectral Range. *ACS Photonics* **2015**, *2*, 1584−1591.
(42) Zhao, H.; Wang, Y.; Capretti, A.; Dal Negro, L.; Klamkin, J. Broadband Electroabsorption Modulators Design Based On Epsilon-Near-Zero Indium Tin Oxide. *IEEE J. Sel. Top. Quantum Electron.* **2015**, *21*, 192−198.
(43) Brewer, S.; Franzen, S. Optical Properties Of Indium Tin Oxide And Fluorine-Doped Tin Oxide Surfaces: Correlation Of Reflectivity, Skin Depth, And Plasmon Frequency With Conductivity. *J. Alloys Compd.* **2002**, *338*, 73−79.
(44) Franzen, S. Surface Plasmon Polaritons And Screened Plasma Absorption In Indium Tin Oxide Compared To Silver And Gold. *J. Phys. Chem. C* **2008**, *112*, 6027−6032.
(45) Wang, Y.; Overvig, A.; Shrestha, S.; Zhang, R.; Wang, R.; Yu, N.; Dal Negro, L. Tunability Of Indium Tin Oxide Materials For Mid-Infrared Plasmonics Applications. *Opt. Mater. Express* **2017**, *7*, 2727.
(46) Wang, Y.; Capretti, A.; Dal Negro, L. Wide Tuning Of The Optical And Structural Properties Of Alternative Plasmonic Materials. *Opt. Mater. Express* **2015**, *5*, 2415.
(47) Yoon, J.; Zhou, M.; Badsha, M.; Kim, T.; Jun, Y.; Hwangbo, C. Broadband Epsilon-Near-Zero Perfect Absorption In The Near-Infrared. *Sci. Rep.* **2015**, *5*, na.
(48) Javani, M.; Stockman, M. Real And Imaginary Properties Of Epsilon-Near-Zero Materials. *Phys. Rev. Lett.* **2016**, *117*, na.
(49) Yariv, A.; Yeh, P. *Photonics*, 1st ed.; Oxford Univ. Press: New York, 2007.
(50) Chen, H. Interference Theory Of Metamaterial Perfect Absorbers. *Opt. Express* **2012**, *20*, 7165.

DOI: 10.1021/acsphotonics.8b00781
ACS Photonics 2018, 5, 3526−3533